# Interfacial instabilities in active viscous films

## R. Alonso-Matilla [a,b], D. Saintillan [a,*]

[a] Department of Mechanical and Aerospace Engineering, University of California San Diego, 9500 Gilman Drive, La Jolla, CA 92093, USA
[b] Department of Chemical Engineering, Columbia University, 500 West 120th Street, New York, NY 10027, USA

**A B S T R A C T**

The interfacial stability of an active viscous film is analyzed theoretically. The film, which rests on a flat substrate and is bounded from above by an air-liquid interface, contains a suspension of active particles such as swimming microorganisms that self-propel, diffuse, and exert active stresses on the suspending Newtonian medium. Using a continuum model for the configuration of the suspension coupled to the forced Stokes equations for the fluid motion, we analyze the growth of linearized normal mode fluctuations with respect to the quiescent base state. In the absence of gravity, puller suspensions are found to be always stable, whereas films containing pushers can become unstable above a critical activity level where active stresses overcome the damping effects of viscosity and surface tension and drive interfacial deformations. Confinement, diffusion and capillary forces all act to stabilize the system, and we characterize the transition to instability in terms of the dimensionless parameters of the problem. We also address the case of inverted films subject to the Rayleigh-Taylor instability, where we demonstrate that active stresses generated by pullers have the ability to stabilize gravitationally unstable films by counteracting the effect of the gravitational body force.

Earnestly strains bloom
hastes the whisperer fluid
swash reverberates

## 1. Introduction

The interaction of active particles with boundaries results in unusual properties that hinge on their ability to self-propel in a noisy environment while inducing local fluid flows. In dilute systems, microswimmers are known to accumulate at walls [1–4] where they display complex trajectories [5,6], swim against external flows [7,8], glide around curved pillars [9], and can show net rectified motion [10,11]. In semi-dilute and concentrated suspensions of pushers, instabilities can be triggered by active stresses resulting from microswimmer disturbances [12–14], with the appearance of coherent structures and the generation of large-scale flows that are chaotic in bulk systems [15] but interact with boundaries in non-trivial ways [16]. Under confinement, these instabilities can lead to spontaneous pumping motions, such as the formation of steady counter-rotating vortices in circular domains [17–19] and the emergence of unidirectional pumping states in periodic channels [19–21], a phenomenon that can be explained based on an apparent reduction in the system's viscosity due to activity [22–24]. The control and regulation of these internally-driven flows, while still in its infancy, could be of great use for the design of microfluidic pumps and flow actuation

devices that rely on active suspensions for the conversion of chemical energy into motion [25] without the need for externally actuated moving parts.

In many biological systems, active materials also come in contact and exchange momentum with soft boundaries. Examples include the spreading of bacterial swarms [26], cell migration during the formation of cancer metastasis [27,28], embryogenesis [29] and wound healing processes [30–33]. In these examples, boundary deformations as a result of active stresses couple back to fluid flows and internal microstructural dynamics, leading in some cases to instabilities and self-organization. Reconstituted systems inspired by cellular dynamics have also been of interest. In one example, Sanchez et al. [34] observed the spontaneous motion of active drops containing a solution of extensile microtubules networks. In a related system, Keber et al. [35] considered active nematics encapsulated inside deformable lipid vesicles, where complex unsteady deformations were reported. These observations have spurred various numerical [36,37] and theoretical [38–41] models for the dynamics of active nematic droplets, either in bulk or on surfaces, where active stresses can result in propulsion, spontaneous division or enhanced spreading. The dynamics of active nematic films and their possible instabilities have also been explored in a few models [42–44]. Our fundamental understanding of the interaction between active suspensions and soft boundaries remains, however, limited.

In this work, we focus on analyzing the forces exerted by a suspension of self-propelled particles on a deformable free surface and their role in driving or stabilizing interfacial instabilities. More specifically, we consider a planar liquid film sitting on a flat substrate and bounded from above by a fluid interface. The film contains a suspension of self-propelled particles, such as swimming microorganisms, which exert active stresses inside the liquid layer as they propel. We use a continuum kinetic theory developed in our previous work [19] to model the configuration of the suspension and its coupling to the mean-field flow, captured by the Stokes equations forced by an active stress tensor. These stresses can generate fluid motions that in turn affect swimmer orientations and can drive the interface out of equilibrium. While our previous work [19] considered instabilities and spontaneous flows in systems confined by rigid boundaries, our focus here is on the coupling of activity with the dynamics of the deformable interface. A linear stability analysis is performed to elucidate the roles of active stresses, viscous damping and capillary forces on the system's stability. As we demonstrate, activity in suspensions of pushers tends to drive interfacial deformations and instabilities, whereas puller suspensions have a stabilizing effect that can in fact help suppress existing instabilities such as the Rayleigh-Taylor instability of an inverted film. Details of the model and governing equations are presented in Section 2, along with their non-dimensionalization in Section 3. The linear stability analysis is set up in Section 4 and results are discussed in Section 5.

## 2. Theoretical model

We analyze the stability of a thin liquid film of an active suspension resting over an infinite planar rigid wall, as depicted in Fig. 1. The suspending fluid is incompressible and Newtonian, with density $\rho$ and dynamic viscosity $\mu$. The film is bounded from above by a deformable air-liquid interface with constant surface tension $\Gamma$, and is subject to a gravitational field with potential $\phi^g = -\rho g z$. We denote by $h_0$ the mean film thickness, and by $z = h(x, y, t)$ the liquid height at position $(x, y)$ as the interface deforms. For simplicity, we restrict our analysis to two-dimensional deformations for which $h \equiv h(x, t)$, and we do not expect the physics to change qualitatively in the more general case. With this parametrization, the unit normal and tangent vectors on the interface are expressed as

$$\mathbf{n} = \frac{(-\partial_x h, 0, 1)}{\sqrt{1 + (\partial_x h)^2}}, \quad \mathbf{t} = \frac{(1, 0, \partial_x h)}{\sqrt{1 + (\partial_x h)^2}}, \tag{1}$$

while the interface curvature is given by

$$\kappa = \nabla \cdot \mathbf{n} = \frac{\partial_{xx} h}{[1 + (\partial_x h)^2]^{1/2}}. \tag{2}$$

The model for the active suspension extends past formulations for bulk and confined microswimmer suspensions [14,19,45], and assumes
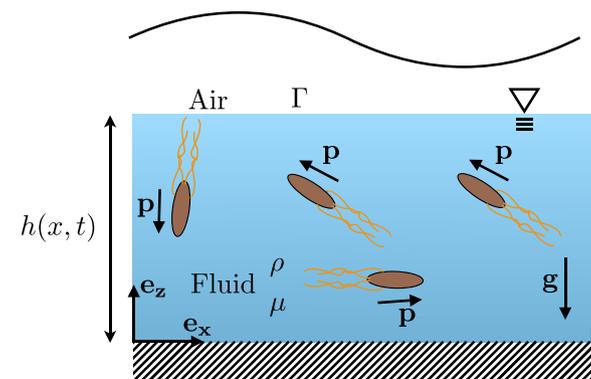


**Fig. 1.** Problem definition: a three-dimensional liquid film of height $h(x, t)$ containing a suspension of microswimmers rests on a flat substrate.

a dilute collection of self-propelled particles with constant swimming velocity $V_0$ oriented along a unit director $\mathbf{p}$. In addition to swimming, the particles are also subject to Brownian motion, with constant translational and rotational diffusivities $d_t$ and $d_r$, respectively. The particles are assumed to be neutrally buoyant; as they swim, they exert active dipolar stresses on the suspending medium, with constant stresslet strength $\sigma_0$ [24,46]. The coefficient $\sigma_0$ is signed and depends on the details of the swimming mechanism; in particular, we distinguish between so-called pushers ($\sigma_0 < 0$), pullers ($\sigma_0 > 0$) and movers ($\sigma_0 = 0$).

The spatial and orientational configuration of the suspension can be described by defining the probability density function $\psi(\mathbf{x}, \mathbf{p}, t)$ of finding a particle at position $\mathbf{x}$, with orientation $\mathbf{p}$ at time $t$. For convenience, we also define its orientational moments over the unit sphere of orientations $\Omega$:

$$c(\mathbf{x}, t) = \int_\Omega \psi(\mathbf{x}, \mathbf{p}, t) \, d\mathbf{p}, \tag{3}$$

$$\mathbf{m}(\mathbf{x}, t) = \int_\Omega \psi(\mathbf{x}, \mathbf{p}, t) \, \mathbf{p} \, d\mathbf{p}, \tag{4}$$

$$\mathbf{D}(\mathbf{x}, t) = \int_\Omega \psi(\mathbf{x}, \mathbf{p}, t) \left( \mathbf{pp} - \frac{\mathbf{I}}{3} \right) d\mathbf{p}, \tag{5}$$

where $c$ is the concentration field, while $\mathbf{m}$ and $\mathbf{D}$ are the unnormalized polarization and nematic tensor fields. Following a standard approach [45], governing equations for these moments can be obtained from the Smoluchowski equation for the probability density function, yielding the coupled set of governing equations

$$\partial_t c = -\nabla \cdot \mathbf{F}_c, \tag{6}$$

$$\partial_t \mathbf{m} = -\nabla \cdot \mathbf{F}_m + \left( \frac{3}{5} \beta \mathbf{E} - \mathbf{W} \right) \cdot \mathbf{m} - 2d_r \mathbf{m}, \tag{7}$$

$$\partial_t \mathbf{D} = -\nabla \cdot \mathbf{F}_D + (\mathbf{D} \cdot \mathbf{W} - \mathbf{W} \cdot \mathbf{D}) - 6d_r \mathbf{D}$$
$$+ \beta \left[ \frac{2}{5} c \mathbf{E} + \frac{3}{7} (\mathbf{E} \cdot \mathbf{D} + \mathbf{D} \cdot \mathbf{E}) - \frac{2}{7} (\mathbf{D} : \mathbf{E}) \mathbf{I} \right], \tag{8}$$

where $\mathbf{F}_c$, $\mathbf{F}_m$ and $\mathbf{F}_D$ denote, respectively, the zeroth, first, and second moments of the translational particle flux:

$$\mathbf{F}_c = V_0 \mathbf{m} + \mathbf{v}c - d_t \nabla c, \tag{9}$$

$$\mathbf{F}_m = V_0 \left( \mathbf{D} + \frac{1}{3} c \mathbf{I} \right) + \mathbf{vm} - d_t \nabla \mathbf{m}, \tag{10}$$

$$\mathbf{F}_D = V_0 \left( \langle \mathbf{ppp} \rangle - \frac{1}{3} \mathbf{mI} \right) + \mathbf{vD} - d_t \nabla \mathbf{D}. \tag{11}$$

Here $\mathbf{v}$ is the fluid velocity, $\mathbf{E} = (\nabla \mathbf{v} + \nabla \mathbf{v}^T)/2$ and $\mathbf{W} = (\nabla \mathbf{v} - \nabla \mathbf{v}^T)/2$ are the rate-of-strain and vorticity tensors, respectively, and $\beta$ is the so-called Bretherton constant [47], which characterizes swimmer shape and is close to 1 for slender particles such as bacteria. The nematic flux $\mathbf{F}_D$ involves the third orientational moment $\langle \mathbf{ppp} \rangle$, for which a closure approximation is needed. Here, we use a common linear closure in terms of the polarization [45]:

$$\langle p_i p_j p_k \rangle = \frac{1}{5} \left[ m_i \delta_{jk} + m_j \delta_{ik} + m_k \delta_{ij} \right], \tag{12}$$

which is a good approximation for orientational distributions that are close to isotropy.

The boundary condition on the particles prescribes no translational flux. As the air-liquid interface is a material surface that moves with the fluid velocity $\mathbf{v}$, we prescribe the no-flux condition on the relative velocity between the interface and the swimmers, leading to the conditions:

$$\mathbf{n} \cdot (\mathbf{F}_c - \mathbf{v}c) = 0 \quad \text{at} \quad z = 0, h(x, t), \tag{13}$$

$$\mathbf{n} \cdot (\mathbf{F}_m - \mathbf{vm}) = \mathbf{0} \quad \text{at} \quad z = 0, h(x, t), \tag{14}$$

$$\mathbf{n} \cdot (\mathbf{F}_D - \mathbf{vD}) = \mathbf{0} \quad \text{at} \quad z = 0, h(x, t), \tag{15}$$

which express the balance of self-propulsion and translational diffusion at the boundaries.

Assuming overdamped dynamics, the fluid velocity field $\mathbf{v}(x, z, t)$ induced by the swimmers satisfies the Stokes equations forced by the active stress contribution $\sigma_0 \nabla \cdot \mathbf{D}$ [24]:

$$\nabla \cdot \mathbf{v} = 0, \tag{16}$$

$$-\nabla p + \mu \nabla^2 \mathbf{v} + \nabla \phi^g + \sigma_0 \nabla \cdot \mathbf{D} = \mathbf{0}. \tag{17}$$

We assume that the velocity satisfies the no-slip condition at the bottom wall $z = 0$. At the free surface, the dynamic boundary condition balances viscous, active and capillary forces:

$$-(\mathbf{T} + \sigma_0 \mathbf{D}) \cdot \mathbf{n} = \Gamma \kappa \, \mathbf{n} \quad \text{at} \quad z = h(x, t), \tag{18}$$

where $\mathbf{T} = -p\mathbf{I} + \mu(\nabla \mathbf{v} + \nabla \mathbf{v}^T)$ is the Newtonian stress tensor in the liquid, and $\kappa(x, t)$ is the local curvature defined in Eq. (2). We also specify a kinematic boundary condition:

$$\partial_t h + u \, \partial_x h = w \quad \text{at} \quad z = h(x, t), \tag{19}$$

which states that the interface moves as a material surface.

## 3. Non-dimensionalization

We proceed to non-dimensionalize both the governing equations and boundary conditions. We scale all the variables using time scale $d_r^{-1}$, length scale $h_0$, velocity scale $h_0 d_r$ and pressure scale $\mu d_r$. The probability distribution function $\psi$ is also scaled by the mean number density $n$. This approach yields five dimensionless groups:

$$\alpha = \frac{\sigma_0 n}{\mu d_r}, \quad G = \frac{\rho g h_0}{\mu d_r}, \quad Ca_{act} = \frac{|\sigma_0| n h_0}{\Gamma}, \quad Pe = \frac{V_0}{d_r h_0}, \quad \Lambda = \frac{d_t d_r}{V_0^2}. \tag{20}$$

The activity parameter $\alpha$ is a dimensionless dipole strength and compares active stresses to the dissipative effects of viscosity and rotational diffusion. The gravitational number $G$ represents the ratio of gravitational forces to viscous forces. The active capillary number $Ca_{act}$ represents the ratio of active forces to capillary forces. The Péclet number $Pe$, which quantifies the level of confinement, compares the persistence length of the swimmers to the film thickness. Finally, $\Lambda$ is a swimmer-specific parameter that compares Brownian diffusion to self-propulsion. For convenience, we also define a viscous capillary number $Ca_{vis} = Ca_{act}/|\alpha| = \mu d_r h_0 / \Gamma$, which quantifies the ratio of viscous forces to capillary forces and will be useful later on when comparing our predictions with classic results for passive viscous films.

Upon scaling, the governing Eqs. (6)–(8) for the moments become

$$\partial_t c = -\nabla \cdot \left[ Pe \mathbf{m} + \mathbf{v} c - \Lambda Pe^2 \nabla c \right], \tag{21}$$

$$\partial_t \mathbf{m} = -\nabla \cdot \left[ Pe \left( \mathbf{D} + \frac{1}{3} c \mathbf{I} \right) + \mathbf{v} \mathbf{m} - \Lambda Pe^2 \nabla \mathbf{m} \right] + \left( \frac{3}{5} \beta \mathbf{E} - \mathbf{W} \right) \cdot \mathbf{m} - 2\mathbf{m}, \tag{22}$$

$$\partial_t \mathbf{D} = -\nabla \cdot \left[ Pe \left( \langle \mathbf{ppp} \rangle - \frac{1}{3} \mathbf{m} \mathbf{I} \right) + \mathbf{v} \mathbf{D} - \Lambda Pe^2 \nabla \mathbf{D} \right] + \beta \left[ \frac{2}{5} c \mathbf{E} + \frac{3}{7} [\mathbf{E} \cdot \mathbf{D} + \mathbf{D} \cdot \mathbf{E}] - \frac{2}{7} (\mathbf{D} : \mathbf{E}) \mathbf{I} \right] + (\mathbf{D} \cdot \mathbf{W} - \mathbf{W} \cdot \mathbf{D}) - 6\mathbf{D}. \tag{23}$$

The dimensionless Stokes equations read

$$\partial_x u + \partial_z w = 0, \tag{24}$$

$$-\partial_x p + [\partial_x^2 u + \partial_z^2 u] + \alpha [\partial_x D_{xx} + \partial_z D_{xz}] = 0, \tag{25}$$

$$-\partial_z p + [\partial_x^2 w + \partial_z^2 w] + \alpha [\partial_x D_{xz} + \partial_z D_{zz}] - G = 0. \tag{26}$$

The kinematic boundary condition of Eq. (19) remains unchanged. The dynamic boundary condition of Eq. (18), after projection along the tangential and normal directions, yields the two conditions at $z = h(x, t)$:

$$\left[ \alpha D_{xz} + \partial_z u + \partial_x w \right] (1 - (\partial_x h)^2) + \left[ \alpha (D_{zz} - D_{xx}) + 4 \partial_z w \right] \partial_x h = 0, \tag{27}$$

and

$$-p[1 + (\partial_x h)^2] - 2\partial_x h \left[ \partial_z u + \partial_x w + \alpha D_{xz} \right] + (\partial_x h)^2 \left[ 2\partial_x u + \alpha D_{xx} \right] + 2\partial_z w + \alpha D_{zz} = |\alpha| Ca_{act}^{-1} \kappa. \tag{28}$$

## 4. Linear stability analysis

We use a temporal linear stability analysis to explore the role of active stresses in driving or suppressing interfacial instabilities. The base state for the analysis is characterized by the absence of flow and a flat interface; it is calculated analytically in Appendix A. We perturb the shape of the interface as a normal mode of the form $h = 1 + \epsilon \hat{h} e^{iKx + St}$ with $\epsilon \ll 1$, where $K = k h_0$ and $S = s/d_r$ are the dimensionless wavenumber and growth rate, respectively. Accordingly, we also perturb the probability distribution function (and hence the orientational moments) as well as the flow variables in the same way: $\psi = \psi^0 + \epsilon \hat{\psi}(z) e^{iKx + St}$, $\mathbf{v} = \epsilon \hat{\mathbf{v}}(z) e^{iKx + St}$, $p = p^0 + \epsilon \hat{p}(z) e^{iKx + St}$, where base state variables are denoted with superscript 0. Following a standard method, we linearize the moment equations retaining terms of order $\epsilon$, and obtain a set of coupled linear ordinary differential equations in $z$ relating the unknown eigenmodes. We omit the full linearized system for brevity. Combined with the linearized kinematic boundary condition $S \hat{h} = \hat{w}$ at $z = 1$, these differential equations, after discretization by a finite volume scheme, can be recast in the form

$$S \mathbf{r} = \mathbf{M}_1 \cdot \mathbf{q}, \tag{29}$$

where the matrix $\mathbf{M}_1$ is defined from the governing equations and boundary conditions, and $\mathbf{r}$ and $\mathbf{q}$ are both vectors of variables that are discretized in space:

$$\mathbf{r} = [\hat{c}, \hat{m}_x, \hat{m}_z, \hat{D}_{xx}, \hat{D}_{xz}, \hat{D}_{zz}, \hat{h}]^T, \tag{30}$$

$$\mathbf{q} = [\hat{c}, \hat{m}_x, \hat{m}_z, \hat{D}_{xx}, \hat{D}_{xz}, \hat{D}_{zz}, \hat{h}, \hat{u}, \hat{w}]^T. \tag{31}$$

Note that the off-diagonal components $\hat{D}_{xy}$ and $\hat{D}_{yz}$ of the nematic order tensor are in general non-zero, but only appear in the problem as non-linear contributions. $\hat{D}_{yy}$ is also non-zero but is easily obtained from $\hat{D}_{xx}$ and $\hat{D}_{zz}$ using the trace-free property of $\hat{\mathbf{D}}$.

In order to transform Eq. (29) into an eigenvalue problem, we express both $\hat{u}$ and $\hat{w}$ in terms of the orientational moments. From the continuity Eq. (24), we first note that

$$\hat{u} = \frac{i}{K} \frac{d\hat{w}}{dz}. \tag{32}$$

Inserting this relation into the $x$ momentum Eq. (25) yields an expression for the pressure:

$$\hat{p} = \frac{1}{K^2} \frac{d^3 \hat{w}}{dz^3} - \frac{d\hat{w}}{dz} + \alpha \hat{D}_{xx} - \frac{i\alpha}{K} \frac{d\hat{D}_{xz}}{dz}. \tag{33}$$

Eqs. (32) and (33) can be substituted into the $z$ momentum Eq. (26) to provide a fourth-order non-homogeneous ODE for the vertical velocity $\hat{w}$ in terms of the nematic tensor components only:

$$\frac{d^4 \hat{w}}{dz^4} - 2K^2 \frac{d^2 \hat{w}}{dz^2} + K^4 \hat{w} = \alpha K^2 \left[ \frac{d\hat{D}_{zz}}{dz} - \frac{d\hat{D}_{xx}}{dz} \right] + i\alpha K \frac{d^2 \hat{D}_{xz}}{dz^2} + i\alpha K^3 \hat{D}_{xz}. \tag{34}$$

The no-slip condition at the bottom wall translates into:

$$\hat{w} = \frac{d\hat{w}}{dz} = 0 \quad \text{at} \quad z = 0. \tag{35}$$

At the free surface $z = 1$, the tangential and normal boundary conditions read

$$\frac{d^2 \hat{w}}{dz^2} + K^2 \hat{w} = i\alpha K \hat{D}_{xz} + \alpha K^2 (D_{xx}^0 - D_{zz}^0) \hat{h}, \tag{36}$$

and

$$-\frac{d^3\hat{w}}{dz^3} + 3K^2\frac{d\hat{w}}{dz} = \alpha K^2(\hat{D}_{xx} - \hat{D}_{zz}) - i\alpha K\frac{d\hat{D}_{xz}}{dz} - \left(GK^2 + |\alpha|Ca_{act}^{-1}K^4\right)\hat{h},$$

(37)

respectively. After discretization, Eqs. (32) and (34), along with boundary conditions (35)–(37), provide a system of algebraic equations for the velocity components in terms of the nematic tensor. After combining these equations with Eq. (29), we obtain an eigenvalue problem of the form $S\mathbf{r} = \mathbf{M}_2 \cdot \mathbf{r}$, where $\mathbf{r}$ was previously defined in Eq. (30) and $\mathbf{M}_2$ is a matrix of dimensions $(6N_z + 1) \times (6N_z + 1)$, where $N_z$ is the number of points used for the discretization of the domain in the vertical direction. This eigenvalue problem is then solved numerically.

## 5. Results and discussion

### 5.1. One-dimensional perturbations

We first analyze the stability to one-dimensional perturbations for which $K = 0$, where we explore the possibility of active stresses driving unidirectional flows within the film. In this limit, the instability is not of interfacial type, the air-liquid interface remains flat, and the variables depend on $z$ only. In this special case, the dynamic boundary condition simplifies to a simple balance between active and viscous stresses. In the base state, presented in Appendix A, there is no flow and particles accumulate at the boundaries as a consequence of the interplay of self-propulsion and diffusion. This accumulation is accompanied by a net wall-normal polarization profile that is antisymmetric with respect to the mid-plane, with particles pointing on average towards the boundary closest to them [4].

Inspection of the linearized equations reveals that unstable eigenmodes only involve the horizontal velocity $\hat{u}$, streamwise polarization $\hat{m}_x$ and component $\hat{D}_{xz}$ of the nematic order tensor; other variables do not appear at linear order. Continuity requires that the vertical velocity $\hat{w}$ vanishes, thus we follow a different procedure to that introduced in Section 4. Instead, we construct, in a similar way, an eigenvalue problem involving the linearized moment equations for $m_x$ and $D_{xz}$, where we make use of the horizontal Stokes momentum equation. We solve the problem numerically. Above a certain level of activity, suspensions of pushers ($\alpha < 0$) develop instabilities with a sequence of unstable modes of increasing complexity. These instabilities are reminiscent of those observed in straight channels [19], with subtle differences arising from the dynamic boundary condition at the free surface. Suspensions of pullers ($\alpha > 0$) are found to be always stable.

The first three unstable modes are illustrated in Fig. 2. In the dominant eigenmode, a non-uniform shear flow develops across the liquid layer. It both fosters and is driven by shear nematic alignment $\hat{D}_{xz}$, which results is an active shear stress profile. It is this feedback loop that is the responsible for the instability in sufficiently thick films and at sufficiently high levels of activity, where active stresses become strong enough to overcome viscous dissipation and rotational diffusion. Because most swimmers in the base state are concentrated near the two boundaries, active stresses are strongest there, which explains the non-uniform shear rate across the film, with a nearly constant velocity profile in the bulk of the film; stronger velocity gradients arise near the boundaries, including at the free surface. This non-uniformity across the film is especially noticeable in weakly diffusive systems (small values of $\Lambda$) in which wall accumulation is strong. It might seem counter-intuitive that the shear rate does not vanish at $z = 1$; this stems from the fact that viscous stresses must balance the tangential active stresses exerted by the nematically aligned bacteria along the interface. In the first unstable mode, the fluid velocity increases monotonically with vertical position, reaching its maximum value at the free surface.
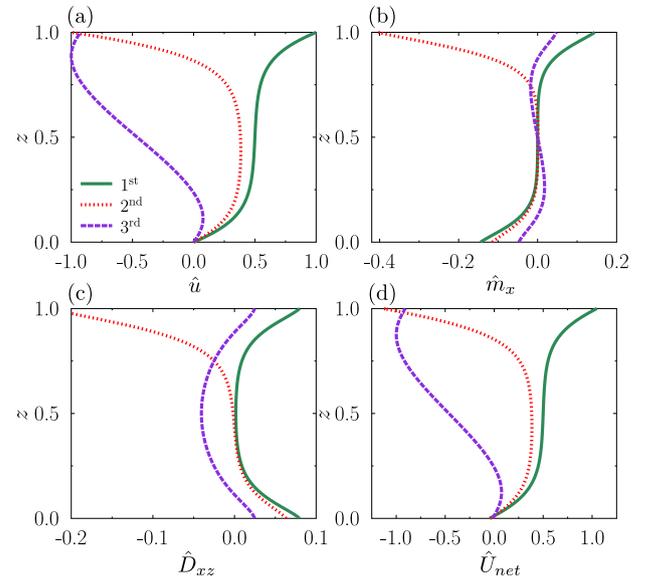


**Fig. 2.** First three unstable eigenmodes for one-dimensional perturbations ($K = 0$) in a suspension of pushers for the choice of parameters: $Pe = 0.5$, $\Lambda = 0.2$ and $\alpha = -50$. Linear unstable modes only involve the horizontal velocity $\hat{u}$ (a), horizontal polarization $\hat{m}_x$ (b) and the off-diagonal component $\hat{D}_{xz}$ of the nematic order tensor (c). The net bacterial horizontal velocity $\hat{U}_{net} = Pe\,\hat{m}_x/c + \hat{u}$, defined as the sum of self-propulsion and advection, is also shown in (d).

Another consequence of the fluid shear across the film is the development of streamwise polarization $\hat{m}_x$. This results from the wall-normal polarization in the base state, which after rotation in the local shear acquires a streamwise component. Given the shear profile, particles near the bottom wall reorient against the flow, as is well known to occur in pressure-driven flow [4] and in spontaneous flows in microfluidic channels [19]; near the free surface, however, streamwise polarization is in the same direction as the flow. This results in an effective population splitting of the particles near the bottom and top surfaces, as was also previously predicted in an imposed shear flow [48]. The net swimmer velocity has contributions from both self-propulsion and advection by the flow: $\hat{U}_{net} = Pe\,\hat{m}_x/c + \hat{u}$. Close to the free surface, both contributions are of the same sign, with the disturbance flow enhancing transport due to swimming. Near the bottom wall, they have opposite signs, and the competition between both effects dictates the net direction of motion. Due to the no-slip condition at the wall, we find that $\hat{U}_{net}$ is slightly negative at the wall, corresponding to the well-known phenomenon of upstream swimming [4,7]. As shown in Fig. 2, additional eigenmodes can also become unstable and involve more complex concentration, alignment and velocity profiles; these higher-order modes, however, have weaker growth rates.

The critical level of activity $\alpha_c$ required for these spontaneous flows to emerge, or marginal stability limit, is plotted vs $Pe$ in Fig. 3, where we also compare it to the case of a planar channel with two no-slip walls [19]. As anticipated, $\alpha_c < 0$ indicating that only pusher suspensions exhibit instabilities. In both cases, the level of activity needed for instability increases with confinement as measured by $Pe$, which is to be expected as viscous damping is more significant in narrow systems. Unsurprisingly, spontaneous flows arise more easily in the presence of a free surface than between two no-slip plates, as the latter cause more dissipation. In very thin films, $\alpha_c$ appears to asymptote to a constant value independent of $Pe$.

### 5.2. Two-dimensional perturbations

We now turn our attention to two-dimensional perturbations for which $K > 0$. Our numerical solution of the eigenvalue problem was first
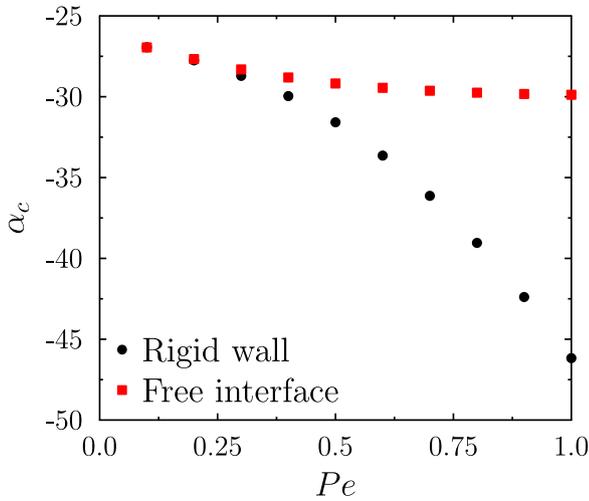
**Fig. 3.** One-dimensional marginal stability limit, showing the critical activity parameter $\alpha_c$ required for the onset of instabilities as a function of the swimming Péclet number *Pe* for two different cases: a fluid film with a rigid wall at the bottom and a free interface on top, and a straight channel with two rigid walls [19]. Parameter values: $\Lambda = 0.5$, $\beta = 1$.
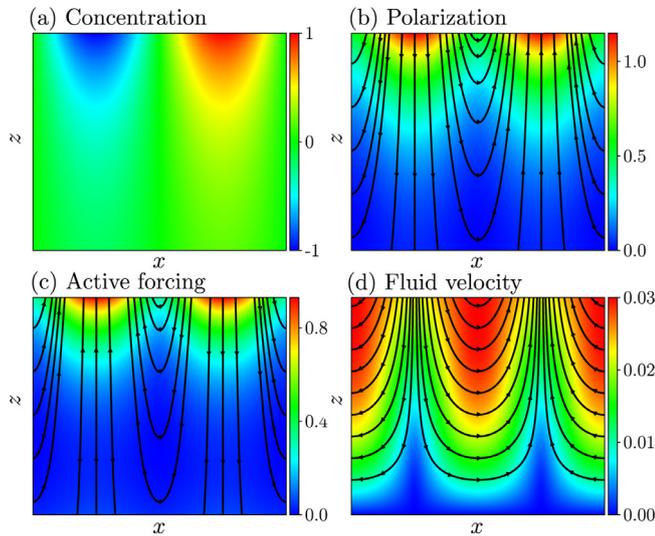


**Fig. 5.** Same quantities as shown in Fig. 4, for a higher activity level: $\alpha = -100$. For this value of $\alpha$, the film is unstable with a positive growth rate $S > 0$. The interface deflection is as shown in Fig. 1, with a crest on the left and a valley on the right.



**Fig. 4.** Dominant two-dimensional eigenmode in a film of a pusher suspension with parameters $\alpha = -1$, $G = 0$, $Ca_{act} = 10$, $K = 1$, $Pe = 1$, $\Lambda = 0.5$, $\beta = 1$. For these parameters, $S < 0$ and the film is stable. The interface deflection is as shown in Fig. 1, with a crest on the left and a valley on the right. The panels show: (a) concentration field $\hat{c}$, (b) polarization field $\hat{\mathbf{m}}$, (c) active forcing term $\alpha \nabla \cdot \hat{\mathbf{D}}$ in the Stokes equations, and (d) fluid velocity $\hat{\mathbf{u}}$. In all cases, colors (blue to red) correspond to the magnitude of the field. (For interpretation of the references to color in this figure legend, the reader is referred to the web version of this article.)

tested in the case of $\alpha = 0$ (passive liquid film with no microswimmers), which can be solved analytically as shown in Appendix B and is unstable for $G < 0$ (inverted film). Perfect agreement between theory and numerics was found in this case. We first discuss results in the absence of gravity ($G = 0$), and as in the case of one-dimensional perturbations we find that instabilities arise only in suspensions of pushers ($\alpha < 0$) and at sufficiently high levels of activity. Figs. 4 and 5 illustrate the eigenmodes corresponding to the largest growth rate for two levels of activity: $\alpha = -1$ (stable), and $-100$ (unstable). In both cases, the interface deflection is as shown in Fig. 1, with a crest on the left and a valley on the right. Under this deflection, particles get squeezed near the valley resulting in a peak in the concentration field $\hat{c}$, whereas a depletion manifests
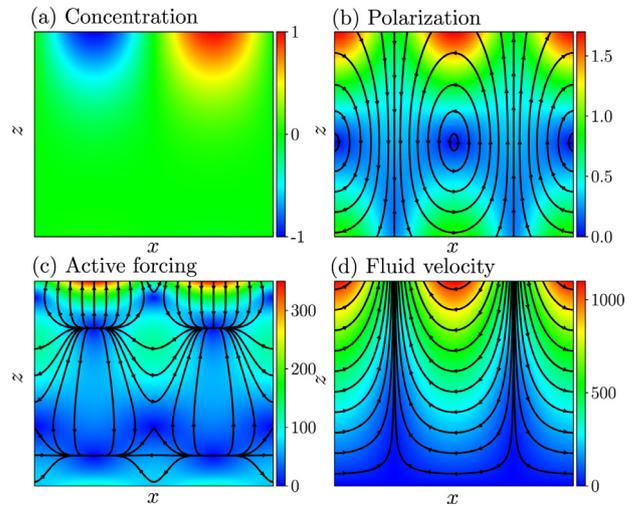
at the crest. The coupling of self-propulsion with the perturbed interface shape along with base-state gradients of the orientational moments promote a decrease in the wall-normal polarization near the peaks of the free surface and an increase near its valleys; streamwise polarization, on the other hand, is maximum at the nodes in between them. In the low-activity case of Fig. 4 ($\alpha = -1$), the active forcing resulting from nematic alignment is fairly weak but is seen to have a destabilizing effect, with an upward push below the interface crest and a downward pull in the valley; this active body force, however, is not sufficient to overcome the stabilizing effect of surface tension, and the flow field indeed shows opposite trends with a downward velocity near the crest and an upward velocity near the valley. As a result, the system is stable and the interface is expected to return to the flat base-state configuration. In the more active case of Fig. 5 ($\alpha = -100$), active stresses are significantly stronger and thus able to overcome capillary forces. This results in a change in the direction of the disturbance flow, which further reinforces shear nematic alignment and leads to an instability, with a net upward flow in the crest of the interface.

More quantitative results are provided in Fig. 6, where the stability of the system is explored in terms of the various dimensionless parameters. The numerical dispersion relation, showing growth rate $S$ as a function of wavenumber $K$, is shown in Fig. 6(a) for different levels of activity. The growth rate is found to plateau at small values of $K$, indicating a long-wave instability in agreement with predictions for unbounded systems [14]. As $K \gtrsim 1$, the growth rate begins to drop and ultimately becomes negative as capillary forces overcome the destabilizing effect of active stresses. Unsurprisingly, stronger activity results in larger growth rates, and also allows for a wider range of wavenumbers to become unstable.

The effects of active capillary number $Ca_{act}$ and Péclet number *Pe* are explored in Fig. 6(b). $Ca_{act}$ can be interpreted as the ratio of destabilizing active forces over stabilizing capillary forces. As a result, the growth rate $S$ is an increasing function of $Ca_{act}$, and typically transitions from negative to positive values as the system becomes unstable. More interesting and less obvious is the dependence on *Pe*, which is a measure of confinement. Increasing *Pe*, i.e., decreasing film thickness, results in enhanced viscous damping due to the bottom no-slip wall. Furthermore, it also causes the two accumulation layers at the wall and free surface to merge, effectively enhancing the role of diffusion. This results in a smoothing of the concentration, polarization, and nematic alignment gradients in the base state. As a consequence of these two
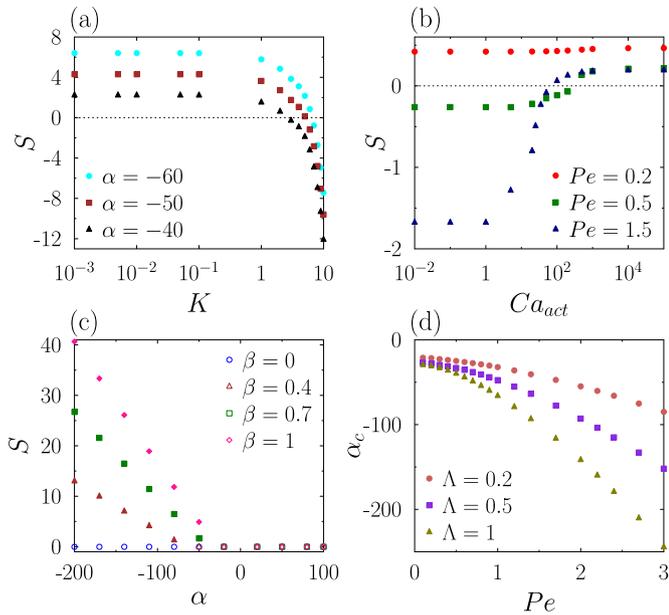
**Fig. 7.** Dependence of the growth rate on the level of activity $\alpha$ for different values of $G$. Note that we are studying the stability of an inverted film (negative gravity). In this case, activity tends to stabilize the film for pullers. Parameter values: $Ca_{vis} = 1$, $K = 1$, $Pe = 1$, $\Lambda = 0.5$, $\beta = 1$.



**Fig. 6.** Stability of the system as a function of the dimensionless parameters of the problem: (a) Growth rate $S$ as a function of wavenumber $K$ for three different values of the activity parameter $\alpha$. Parameter values: $G = 0$, $Ca_{act} = 10$, $Pe = 0.5$, $\Lambda = 0.5$, $\beta = 1$. (b) Growth rate $S$ as a function of the active capillary number $Ca_{act}$ for three different values of the Péclet number $Pe$. Parameter values: $G = 0$, $\alpha = -30$, $K = 1$, $\Lambda = 0.5$, $\beta = 1$. (c) Growth rate $S$ as a function of the activity parameter $\alpha$ for four different values of the Bretherton constant $\beta$, with $\beta = 0$ and 1 corresponding to spheres and slender swimmers, respectively. Parameter values: $Ca_{act} = 100$, $G = 0$, $K = 1$, $Pe = 0.2$, $\Lambda = 0.5$. Solid symbols and empty symbols correspond to unstable and stable systems, respectively. (d) Marginal stability, showing the critical activity level $\alpha_c$ for instability as a function of Péclet number $Pe$ for three different values of the swimmer parameter $\Lambda$. Parameter values: $G = 0$, $Ca_{act} = 0.1$, $K = 1$, $\beta = 1$.

effects, increasing $Pe$ tends to stabilize the system, and this trend is especially visible at low values of $Ca_{act}$.

As discussed previously, instabilities arise from active stresses, which hinge on the nematic alignment of the microswimmers in their self-generated fluid flows. To confirm this mechanism, we consider the effect of swimmer shape in Fig. 6(c), where the growth rate is plotted as a function of $\alpha$ for different values of the Bretherton constant $\beta$, ranging from spheres to needles. In the case of spherical swimmers ($\beta = 0$), reorientation comes from vorticity only, and thus nematic alignment is very weak, being induced by the presence of the boundaries rather than by the flow. Consequently, active flows are weak too and we find that the system is always stable regardless of the value of $\alpha$. Departures from the spherical shape lead to swimmer reorientation by both the local vorticity and rate of strain, resulting in more significant nematic alignment and active stresses. This results in a positive growth rate in pusher suspensions at high activity levels, which increases as the aspect ratio of the particles increases ($\beta \to 1$).

The transition to instability is further characterized in Fig. 6(d), where we show the marginal stability curves as functions of $Pe$ for different values of $\Lambda$. Increasing either $Pe$ (confinement) or $\Lambda$ (diffusion) tends to smooth out gradients in nematic alignment, and hence the critical level of activity increases in absolute value. Interestingly, $\alpha_c$ does not plateau at large $Pe$ as in the case of one-dimensional perturbations in Fig. 3. We attribute this difference to the recirculating flows that emerge in two dimensions, which are more strongly damped by viscous effects as film thickness decreases.

In all the results presented so far, we found that suspensions of pushers can destabilize active films at sufficiently high values of $|\alpha|$, whereas pullers do not. To further emphasize the stabilizing quality of puller sus-
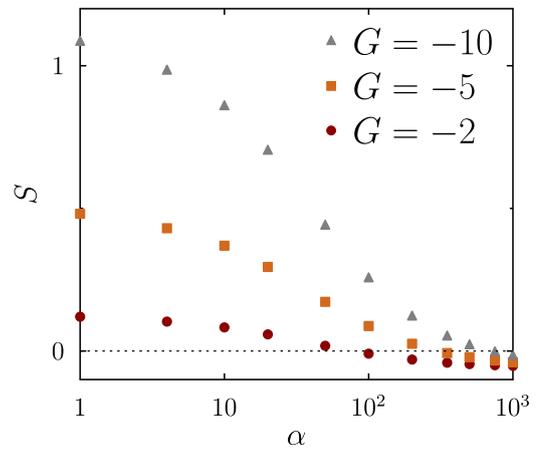
pensions, we now consider their effect on the gravitational instability of an inverted film in which $G < 0$. In the absence of swimmers, such films destabilize by the classic Rayleigh-Taylor instability, with a positive growth rate at long wavelengths that can be calculated analytically as shown in Appendix B. When puller particles are added, a decrease in growth rate occurs as a result of activity as shown in Fig. 7. At very high activity levels, the growth rate in fact becomes negative, showing that puller suspensions have the ability to stabilize gravitational instabilities by nematically aligning and exerting active stresses that counteract the gravitational body force. This curious finding highlights the subtle effect of active stresses in puller suspensions, which have received limited attention in past work.

## Acknowledgments

## Appendix A. Analytical solution for the equilibrium state

We derive an analytical solution for the equilibrium configuration inside the film, which also serves as base state for the linear stability analysis. In this configuration, there is no fluid flow ($u^0 = w^0 = 0$) and the variables only depend on $z$. Symmetry also dictates that $m_x^0 = D_{xz}^0 = D_{zx}^0 = 0$. In the base state, both boundaries are equivalent, leading to a symmetric distribution across the film which is identical to that between two rigid plates [4]. Consequently, it is convenient in the following calculation to choose the origin for the $z$ axis at the film centerline.

*Pressure gradient*

In the base state, a pressure gradient develops to balance the gravitational body force and normal active stresses. In dimensionless form, the $z$ momentum equation is written

$$\frac{dp^0}{dz} = \alpha \frac{dD_{zz}^0}{dz} - G. \tag{A.1}$$

*Orientational moments*

After simplifications, the governing Eqs. (21)–(23) for the orientational moments read

$$-Pe \frac{dm_z^0}{dz} + \Lambda Pe^2 \frac{d^2 c^0}{dz^2} = 0, \tag{A.2}$$

$$-Pe\left(\frac{dD_{zz}^0}{dz} + \frac{1}{3}\frac{dc^0}{dz}\right) + \Lambda Pe^2\frac{d^2m_z^0}{dz^2} - 2m_z^0 = 0, \tag{A.3}$$

$$-\frac{4Pe}{15}\frac{dm_z^0}{dz} + \Lambda Pe^2\frac{d^2D_{zz}^0}{dz^2} - 6D_{zz}^0 = 0, \tag{A.4}$$

subject to the following no-flux conditions at the solid-fluid and air-fluid interfaces:

$$-Pem_z^0 + \Lambda Pe^2\frac{dc^0}{dz} = 0 \quad \text{at} \quad z = \pm\frac{1}{2}, \tag{A.5}$$

$$-Pe\left(D_{zz}^0 + \frac{1}{3}c^0\right) + \Lambda Pe^2\frac{dm_z^0}{dz} = 0 \quad \text{at} \quad z = \pm\frac{1}{2}, \tag{A.6}$$

$$-\frac{4Pe}{15}m_z^0 + \Lambda Pe^2\frac{dD_{zz}^0}{dz} = 0 \quad \text{at} \quad z = \pm\frac{1}{2}. \tag{A.7}$$

To close the system, we also impose the normalization condition:

$$\int_{-1/2}^{1/2} c(z)dz = 1. \tag{A.8}$$

Integrating Eq. (A.2) and making use of Eq. (A.5) to determine the constant of integration, we get:

$$m_z^0(z) = \Lambda Pe\frac{dc^0}{dz}, \tag{A.9}$$

which states that the vertical swimming and diffusive fluxes are everywhere balanced in the film [4]. Plugging this result into Eq. (A.3) and integrating again yields:

$$D_{zz}^0(z) = \Lambda^2 Pe^2\frac{d^2c^0}{dz^2} - \left(2\Lambda + \frac{1}{3}\right)c^0 - A_1, \tag{A.10}$$

where $A_1$ is a constant of integration. Eqs. (A.9) and (A.10) express both the wall-normal polarization $m_z^0$ and nematic order parameter $D_{zz}^0$ in terms of the concentration field $c^0$. To determine $c^0$, we insert Eqs. (A.9) and (A.10) into Eq. (A.4) and rearrange terms to obtain a fourth-order non-homogeneous differential equation:

$$\frac{d^4c^0}{dz^4} - (\zeta^2 + v^2)\frac{d^2c^0}{dz^2} + \zeta^2 v^2 c^0 = -\frac{6A_1}{\Lambda^3 Pe^4}, \tag{A.11}$$

where

$$\zeta = \frac{\left(8\Lambda + 3/5 + \sqrt{16\Lambda^2 + 8\Lambda/5 + 9/25}\right)^{1/2}}{\sqrt{2}\Lambda Pe}, \tag{A.12}$$

$$v = \frac{\left(8\Lambda + 3/5 - \sqrt{16\Lambda^2 + 8\Lambda/5 + 9/25}\right)^{1/2}}{\sqrt{2}\Lambda Pe}. \tag{A.13}$$

Taking into account the symmetry of the problem, the general solution of Eq. (A.11) can be found as

$$c^0(z) = c_p + A_2\cosh\zeta z + A_3\cosh vz, \tag{A.14}$$

where $c_p$ is the particular solution, and $A_2$ and $A_3$ are constants of integration to be determined. The general solutions for $m_z^0$ and $D_{zz}^0$ are then respectively:

$$m_z^0(z) = A_2\Lambda Pe\zeta\sinh\zeta z + A_3\Lambda Pe v\sinh vz, \tag{A.15}$$

$$D_{zz}^0(z) = A_2(\Lambda^2 Pe^2\zeta^2 - 2\Lambda - 1/3)\cosh\zeta z$$
$$+ A_3(\Lambda^2 Pe^2 v^2 - 2\Lambda - 1/3)\cosh vz. \tag{A.16}$$

The constants $c_p$, $A_2$ and $A_3$ are determined using conditions (A.6)–(A.8):

$$A_2 = \frac{v\sinh\frac{v}{2}(\Lambda^2 Pe^2 v^2 - 2\Lambda - 3/5)}{\Omega_1 - \Omega_2}, \tag{A.17}$$

$$A_3 = -\frac{\zeta\sinh\frac{\zeta}{2}(\Lambda^2 Pe^2\zeta^2 - 2\Lambda - 3/5)}{\Omega_1 - \Omega_2}, \tag{A.18}$$

$$c_p = 6\Lambda\left[A_2\cosh\frac{\zeta}{2} + A_3\cosh\frac{v}{2}\right], \tag{A.19}$$

where

$$\Omega_1 = v\sinh\frac{v}{2}\left(6\Lambda\cosh\frac{\zeta}{2} + \frac{2}{\zeta}\sinh\frac{\zeta}{2}\right) \times [\Lambda^2 Pe^2 v^2 - 2\Lambda - 3/5], \tag{A.20}$$

$$\Omega_2 = \zeta\sinh\frac{\zeta}{2}\left(6\Lambda\cosh\frac{v}{2} + \frac{2}{v}\sinh\frac{v}{2}\right) \times [\Lambda^2 Pe^2\zeta^2 - 2\Lambda - 3/5]. \tag{A.21}$$

The analytical solution obtained here was compared to a numerical solution of the governing equations obtained by finite volumes, and perfect agreement was found.

## Appendix B. Stability analysis for a passive liquid film

In this appendix, we carry out the linear stability analysis for a passive viscous film in which no microswimmers are present. In this case, the analysis is performed directly on the Stokes equations (24)–(26) and boundary conditions where we set $\alpha = 0$, and is amenable to an analytical solution. Taking the divergence of the momentum equation shows that the pressure is harmonic, with general solution

$$\hat{p} = C_{p1}e^{Kz} + C_{p2}e^{-Kz}, \tag{B.1}$$

where $C_{p1}$ and $C_{p2}$ are constants of integration. Plugging this solution into Eqs. (25)–(26) and integrating yields expressions for the velocity eigenfunctions $\hat{u}$ and $\hat{w}$:

$$\hat{u} = C_{u1}e^{Kz} + C_{u2}e^{-Kz} + C_{u3}ze^{Kz} + C_{u4}ze^{-Kz}, \tag{B.2}$$

$$\hat{w} = C_{w1}e^{Kz} + C_{w2}e^{-Kz} + C_{w3}ze^{Kz} + C_{w4}ze^{-Kz}, \tag{B.3}$$

where

$$C_{u3} = \frac{iC_{p1}}{2K}, \quad C_{u4} = -\frac{iC_{p2}}{2K}, \tag{B.4}$$

$$C_{w3} = \frac{C_{p1}}{2K^2}, \quad C_{w4} = \frac{C_{p2}}{2K^2}. \tag{B.5}$$

Applying continuity and the no-slip boundary condition at the bottom wall provides four additional relationships:

$$C_{u1} = \frac{i(C_{p1} - C_{p2})}{4K^2}, \quad C_{u2} = -\frac{i(C_{p1} - C_{p2})}{4K^2}, \tag{B.6}$$

$$C_{w1} = -\frac{C_{p1} + C_{p2}}{4K^3}, \quad C_{w2} = \frac{C_{p1} + C_{p2}}{4K^3}. \tag{B.7}$$

We can now apply the kinematic boundary condition Eq. (19) as well as the tangential and normal dynamic boundary conditions Eqs. (27)–(28), where we note that $|\alpha|Ca_{act}^{-1} = Ca_{vis}^{-1}$. Upon inserting Eqs. (B.1)–(B.3) along with relations (B.4)–(B.7), we arrive at a system of three equations involving $C_{p1}$, $C_{p2}$, $\hat{h}$ and $S$:

$$\left[\frac{e^K}{2K^2} - \frac{\sinh K}{2K^3}\right]C_{p1} + \left[-\frac{\sinh K}{2K^3} + \frac{e^{-K}}{2K^2}\right]C_{p2} = S\hat{h}, \tag{B.8}$$

$$\left[e^K + \frac{\cosh K}{K}\right]C_{p1} + \left[e^{-K} - \frac{\cosh K}{K}\right]C_{p2} = 0, \tag{B.9}$$

$$\left[Ke^K - \cosh K\right]C_{p1} + \left[-Ke^{-K} - \cosh K\right]C_{p2} = -\left[GK^2 + Ca_{vis}^{-1}K^4\right]\hat{h}. \tag{B.10}$$

These can be combined to eliminate $C_{p1}$, $C_{p2}$ and $\hat{h}$. This provides the dispersion relation for the growth rate $S$ in terms of the parameters of

the problem $K$, $Ca_{vis}$ and $G$:

$$S = \frac{2K - \sinh(2K)}{4K(K^2 + \cosh^2 K)}\left(G + K^2 Ca_{vis}^{-1}\right). \tag{B.11}$$

This expression is in agreement with the previous result of Yiantsios and Higgins [49] in the special case of negligible air density and viscosity. The prefactor in this expression can be shown to be negative for all values of $K$. The effect of surface tension is therefore always stabilizing in planar films, and the larger the wavenumber the stronger the capillary restoring force. Gravity can be destabilizing in inverted films for which $G < 0$, corresponding to the Rayleigh-Taylor instability. The effect of gravity is strongest at low wavenumbers, with the buoyancy force in inverted films tending to pull the bulge of the interface further down and amplify the shape perturbation. In this case, there is a critical viscous capillary number $Ca_{vis}^c = K^2/G$ for the instability to occur. In the two limits of $K \to 0$ and $K \to \infty$, the dispersion relation simplifies to:

$$S(K \to 0) = -\frac{K^2}{3}\left(G + K^2 Ca_{vis}^{-1}\right), \tag{B.12}$$

$$S(K \to \infty) = -\frac{1}{2K}\left(G + K^2 Ca_{vis}^{-1}\right). \tag{B.13}$$

## Supplementary material

Supplementary material associated with this article can be found, in the online version, at doi:10.1016/j.jnnfm.2019.06.004.

## References

[1] A.P. Berke, L. Turner, H.C. Berg, E. Lauga, Hydrodynamic attraction of swimming microorganisms by surfaces, Phys. Rev. Lett. 101 (2008) 038102.
[2] T. Kaya, H. Koser, Characterization of hydrodynamic surface interactions of *Escherichia coli* cell bodies in shear flow, Phys. Rev. Lett. 103 (2009) 138103.
[3] G. Li, J.X. Tang, Accumulation of microswimmers near a surface mediated by collision and rotational Brownian motion, Phys. Rev. Lett. 103 (2009) 078101.
[4] B. Ezhilan, D. Saintillan, Transport of a dilute active suspension in pressure-driven channel flow, J. Fluid Mech. 777 (2015) 482–522.
[5] W.R. DiLuzio, L. Turner, M. Mayer, P. Garstecki, D.B. Weibel, H.C. Berg, G.M. Whitesides, *Escherichia coli* swim on the right-hand side, Nature 435 (2005) 1271–1274.
[6] E. Lauga, W.R. DiLuzio, G.M. Whitesides, H.A. Stone, Swimming in circles: motion of bacteria near solid boundaries, Biophys. J. 90 (2006) 400–412.
[7] T. Kaya, H. Koser, Direct upstream motility in *E. coli*, Biophys. J. 102 (2012) 1514–1523.
[8] D.J. Kantsler V., M. Blayney, R.E. Goldstein, Rheotaxis facilitates upstream navigation of mammalian sperm cells, Elife 3 (2014) e02403.
[9] T. Takagi, J. Palacci, A.B. Braunschweig, M.J. Shelley, J. Zhang, Hydrodynamic capture of microswimmers into sphere-bound orbits, Soft Matter 10 (2014) 1784–1789.
[10] M. Davies Wykes, X. Zhong, J. Tong, T. Adachi, Y. Liu, L. Ristroph, M. Ward, M. Shelley, J. Zhang, Guiding microscale swimmers using teardrop-shaped posts, Soft Matter 13 (2017) 4681–4688.
[11] J. Tong, M. Shelley, Directed migration of microscale swimmers by an array of shaped obstacles: modeling and shape optimization, SIAM J. Appl. Math. 78 (2018) 2370–2392.
[12] R.A. Simha, S. Ramaswamy, Hydrodynamic fluctuations and instabilities in ordered suspensions of self-propelled particles, Phys. Rev. Lett. 89 (2002) 058101.
[13] D. Saintillan, M.J. Shelley, Orientational order and instabilities in suspensions of self-locomoting rods, Phys. Rev. Lett. 99 (2007) 058102.
[14] D. Saintillan, M.J. Shelley, Instabilities and pattern formation in active particle suspensions: kinetic theory and continuum simulations, Phys. Rev. Lett. 100 (2008) 178103.
[15] D. Saintillan, M.J. Shelley, Emergence of coherent structures and large-scale flows in motile suspensions, J. R. Soc. Interface (2011). rsif20110355.
[16] M. Theillard, D. Saintillan, Computational mean-field modeling of confined active fluids, submitted (2019).
[17] H. Wioland, F.G. Woodhouse, J. Dunkel, J.O. Kessler, R.E. Goldstein, Confinement stabilizes a bacterial suspension into a spiral vortex, Phys. Rev. Lett. 110 (2013) 268102.
[18] E. Lushi, H. Wioland, R.E. Goldstein, Fluid flows created by swimming bacteria drive self-organization in confined suspensions, Proc. Natl. Acad. Sci. USA 111 (2014) 9733–9738.
[19] M. Theillard, R. Alonso-Matilla, D. Saintillan, Geometric control of active collective motion, Soft Matter 13 (2017) 363–375.
[20] H. Wioland, E. Lushi, R.E. Goldstein, Directed collective motion of bacteria under channel confinement, New J. Phys. 18 (2015) 075002.
[21] A. Creppy, F. Plouraboué, O. Praud, X. Druart, S. Cazin, Symmetry-breaking phase transitions in highly concentrated semen, J. R. Soc. Interface 13 (2016) 20160575.
[22] D. Saintillan, The dilute rheology of swimming suspensions: a simple kinetic model, Exp. Mech. 50 (2010) 1275–1281.
[23] R. Alonso-Matilla, B. Ezhilan, D. Saintillan, Microfluidic rheology of active particle suspensions: Kinetic theory, Biomicrofluidics 10 (2016) 043505.
[24] D. Saintillan, Rheology of active fluids, Annu. Rev. Fluid Mech. 50 (2018) 563–592.
[25] G. Vizsnyiczai, G. Frangipane, C. Maggi, F. Saglimbeni, B. S., R. Di Leonardo, Light controlled 3D micromotors powered by bacteria, Nature Comm. 8 (2017) 15974.
[26] A.E. Patteson, A. Gopinath, P.E. Arratia, The propagation of active-passive interfaces in bacterial swarms, Nature Comm. 9 (2018) 5373.
[27] A. Nürnberg, T. Kitzing, R. Grosse, Nucleating actin for invasion, Nat. Rev. Cancer 11 (2011) 177.
[28] D. Hoshino, K.M. Branch, A.M. Weaver, Signaling inputs to invadopodia and podosomes, J. Cell Sci. 126 (2013) 2979–2989.
[29] P. Martin, S.M. Parkhurst, Parallels between tissue repair and embryo morphogenesis, Development 131 (2004) 3021–3034.
[30] J. Sherratt, J. Murray, Mathematical analysis of a basic model for epidermal wound healing, J. Math. Biol. 29 (1991) 389–404.
[31] P.D. Dale, P.K. Maini, J.A. Sherratt, Mathematical modeling of corneal epithelial wound healing, Math. Biosci. 124 (1994) 127–147.
[32] S. Mark, R. Shlomovitz, N.S. Gov, M. Poujade, E. Grasland-Mongrain, P. Silberzan, Physical model of the dynamic instability in an expanding cell culture, Biophys. J. 98 (2010) 361–370.
[33] J. Zimmermann, M. Basan, H. Levine, An instability at the edge of a tissue of collectively migrating cells can lead to finger formation during wound healing, Eur. Phys. J. Spec. Top. 223 (2014) 1259–1264.
[34] T. Sanchez, D.T. Chen, S.J. DeCamp, M. Heymann, Z. Dogic, Spontaneous motion in hierarchically assembled active matter, Nature 491 (2012) 431–434.
[35] F.C. Keber, E. Loiseau, T. Sanchez, S.J. DeCamp, L. Giomi, M.J. Bowick, M.C. Marchetti, Z. Dogic, A.R. Bausch, Topology and dynamics of active nematic vesicles, Science 345 (2014) 1135–1139.
[36] E. Tjhung, D. Marenduzzo, M.E. Cates, Spontaneous symmetry breaking in active droplets provides a generic route to motility, Proc. Natl. Acad. Sci. USA 109 (2012) 12381–12386.
[37] T. Gao, Z. Li, Self-driven droplet powered by active nematic, Phys. Rev. Lett. 119 (2017) 108002.
[38] J.-F. Joanny, S. Ramaswamy, A drop of active matter, J. Fluid Mech. 705 (2012) 46–57.
[39] L. Giomi, A. DeSimone, Spontaneous division and motility in active nematic droplets, Phys. Rev. Lett. 112 (2014) 147802.
[40] C.A. Whitfield, D. Marenduzzo, R. Voituriez, R.J. Hawkins, Active polar fluid flow in finite droplets, Eur. Phys. J. E 37 (2014) 1–15.
[41] D. Khoromskaia, G.P. Alexander, Motility of active fluid drops on surfaces, Phys. Rev. E 92 (2015) 062311.
[42] R. Voituriez, J. Joanny, J. Prost, Generic phase diagram of active polar films, Phys. Rev. Lett. 96 (2006) 028102.
[43] S. Sankararaman, S. Ramaswamy, Instabilities and waves in thin films of living fluids, Phys. Rev. Lett. 102 (2009) 118107.
[44] M.L. Blow, M. Aqil, B. Liebchen, D. Marenduzzo, Motility of active nematic films driven by "active anchoring", Soft Matter 13 (2017) 6137–6144.
[45] D. Saintillan, M.J. Shelley, Active suspensions and their nonlinear models, C. R. Physique 14 (2013) 497–517.
[46] Y. Hatwalne, S. Ramaswamy, M. Rao, R.A. Simha, Rheology of active-particle suspensions, Phys. Rev. Lett. 92 (2004) 118101.
[47] F.P. Bretherton, The motion of rigid particles in a shear flow at low Reynolds number, J. Fluid Mech. 14 (1962) 284–304.
[48] H. Nili, M. Kheyri, J. Abazari, A. Fahimniyabd, A. Naji, Population splitting of rodlike swimmers in Couette flow, Soft Matter 13 (2017) 4494–4506.
[49] S.G. Yiantsios, B.G. Higgins, Rayleigh–Taylor instability in thin viscous films, Phys. Fluids 1 (1989) 1484–1501.